High-speed Lissajous-scan atomic force microscopy: Scan pattern planning and control design issues

A. Bazaei,[a] Yuen K. Yong,[b] and S. O. Reza Moheimani[c]
School of Electrical Engineering and Computer Science, The University of Newcastle, Callaghan, NSW 2308, Australia

(Received 5 March 2012; accepted 17 May 2012; published online 4 June 2012)

Tracking of triangular or sawtooth waveforms is a major difficulty for achieving high-speed operation in many scanning applications such as scanning probe microscopy. Such non-smooth waveforms contain high order harmonics of the scan frequency that can excite mechanical resonant modes of the positioning system, limiting the scan range and bandwidth. Hence, fast raster scanning often leads to image distortion. This paper proposes analysis and design methodologies for a nonlinear and smooth closed curve, known as Lissajous pattern, which allows much faster operations compared to the ordinary scan patterns. A simple closed-form measure is formulated for the image resolution of the Lissajous pattern. This enables us to systematically determine the scan parameters. Using internal model controllers (IMC), this non-raster scan method is implemented on a commercial atomic force microscope driven by a low resonance frequency positioning stage. To reduce the tracking errors due to actuator nonlinearities, higher order harmonic oscillators are included in the IMC controllers. This results in significant improvement compared to the traditional IMC method. It is shown that the proposed IMC controller achieves much better tracking performances compared to integral controllers when the noise rejection performances is a concern. © *2012 American Institute of Physics*. [http://dx.doi.org/10.1063/1.4725525]

I. INTRODUCTION

Use of triangular or sawtooth signals for raster scanning has been the standard method of scanning employed in all kinds of scanning probe microscopy (SPM (Ref. 1)), such as STM,[2] AFM,[3] and SNONM.[4] Such waveforms have also been used in other probe-based emerging technologies. For example, in Refs. 5 and 6, where digital data are recorded by an array of probes, the motion is conducted in a raster pattern within the storage area. Characteristics of the reference signals to be tracked during raster scanning can cause considerable control difficulties in SPMs. In conventional raster scanning, the positioning stage has to follow a triangle or sawtooth waveform in one axis, while the other axis has to follow a ramp or staircase signal. Although this method can provide acceptable solutions during slow operations, it cannot provide satisfactory responses in fast scan regimes. There has been a growing demand for high-speed atomic force microscopy, particularly to study dynamic behavior of biological samples.[7,8]

In addition to its fundamental frequency, the spectrum of a triangle or sawtooth waveform contains strong higher order harmonics. When these waveforms are used as reference signals, the limited mechanical bandwidth of SPM positioning stages along with their highly resonant nature and actuation limitations and nonlinearities do not allow for the requisite high-speed performance. For an acceptable performance in conventional raster scanning, the frequency of the raster signal is typically limited to 1% of the first resonance frequency of the positioning stage. This constraint ensures acceptable tracking of high order harmonics of the raster signal without exciting the vibration modes of the stage. However, this leads to a low scan speed and an image that takes several minutes to develop.

To enhance the scan speed in SPMs, a variety of solutions has been offered. One approach is to use feedback to increase the damping ratio of the lightly damped poles of the SPM positioning stage.[9–11] This method removes the possibility of exciting the mechanical resonance modes of the stage by the raster signal. However, the mechanical bandwidth of the scanner, which must accommodate the scan frequency as well as its 6–7 harmonics, remains limited. In Refs. 12–16, feedforward control methods are used to improve the tracking performance in the presence of limited mechanical bandwidth of the positioning stage. Design of sophisticated structures for positioning stages, whose first modes are located at very high frequencies (beyond 10 kHz), is getting more attraction.[17–20] Non-raster scanning methods have been recently proposed to considerably increase the scan speed of SPMs. These methods are based on using spiral[21,22] and cycloid-like patterns[23] by tracking sinusoidal reference signals on x and y axes of the positioning stage. Tracking of sinusoidal signals in a highly resonant stage with low mechanical bandwidth is a much easier proposition than tracking of a triangle or sawtooth reference with the same amplitude and fundamental frequency.

This paper considers an alternative non-raster scan method, based on Lissajous pattern. In contrast to spiral and cycloid scan methods, which involve tracking of slow ramp signals in addition to the sinusoidal references, this method forces the scanner lateral axes to follow purely sinusoidal

a)Electronic mail: ali.bazaei@newcastle.edu.au.
b)Electronic mail: yuenkuan.yong@newcastle.edu.au.
c)Electronic mail: reza.moheimani@newcastle.edu.au.

 © 2012 American Institute of Physics

Downloaded 04 Jun 2012 to 134.148.216.165. Redistribution subject to AIP license or copyright; see http://rsi.aip.org/about/rights_and_permissions

waveforms with fixed amplitudes and identical phases. Frequencies of the sinusoids are fixed. However, their small difference significantly affects the shape, the resolution, and the scan time of the pattern. Using a commercial SPM, we show that the method can obtain high-quality images at high scan speeds, where regular raster scanning approach cannot perform acceptably. A mathematical analysis of the Lissajous pattern is presented and a closed-form formula is derived to, *a priori*, determine the resolution of the pattern. The analysis provides a systematic and straightforward procedure to determine the parameters of the Lissajous pattern, based on desired raster dimensions, resolution, and lateral frequencies of the scanner. To track the sinusoidal references, we used novel versions of internal model controllers (IMC), where higher order harmonics of the sinusoids are included in the controllers to improve the residual tracking errors due to nonlinearities of piezoelectric actuators. We also show that when the noise attenuation performance of the control system is limited, the IMC methods provide much better tracking performances for sinusoidal references compared to integral controllers.

The rest of the paper continues as follows. Sec. II A presents a thorough analysis of the Lissajous pattern, which leads to a measure of resolution and a systematic design procedure. In Sec. III, we compare the Lissajous method with conventional raster scanning and investigate the performance of the proposed method using a commercial atomic force microscope and internal model controllers.

II. LISSAJOUS PATTERN

The Lissajous-scan pattern can be generated by forcing the x and y axes of the scanner to track the following signals:

$$x(t) = A_x \cos(\omega_x t); \quad y(t) = A_y \cos(\omega_y t), \tag{1}$$

where $\omega_x = 2\pi f_x$, $\omega_y = 2\pi f_y$, and A_x and A_y are positive constants representing the frequencies and amplitudes of the sinusoidal signals associated with x and y axes, respectively. Assuming that the scanner is a parallel-kinematics device with identical axes, and assuming that the frequency range of interest is sufficiently far away from the scanner's resonance frequency, the above signals, or a scaled version of them, can be directly applied to the x and y axis actuators. Otherwise, the gains and phases associated with the two channels can be compensated using either a feedforward controller, or preferably a feedback controller. Efficient control design methodologies for tracking of sinusoidal set points exist in the literature.[24] In experiments reported here, the AFM scanner is a piezoelectric tube nanopositioner, which is a parallel-kinematics device.[25]

In Eq. (1), the frequency difference between ω_x and ω_y determines the overall shape of the Lissajous pattern and the period in which the pattern progresses and repeats itself.[26,27] The phase difference between the sinusoids, which is assumed zero in this paper for simplicity, has also an impact on the shape of the pattern.[26] Numerous scan patterns can be generated by selecting frequencies and phase shifts of the two sinusoids in Eq. (1). Here we have opted to choose $f_x = 100$ Hz, $f_y = 99$ Hz, and unity amplitudes such that a pattern, as shown in Fig. 1, is obtained, leading to a square-

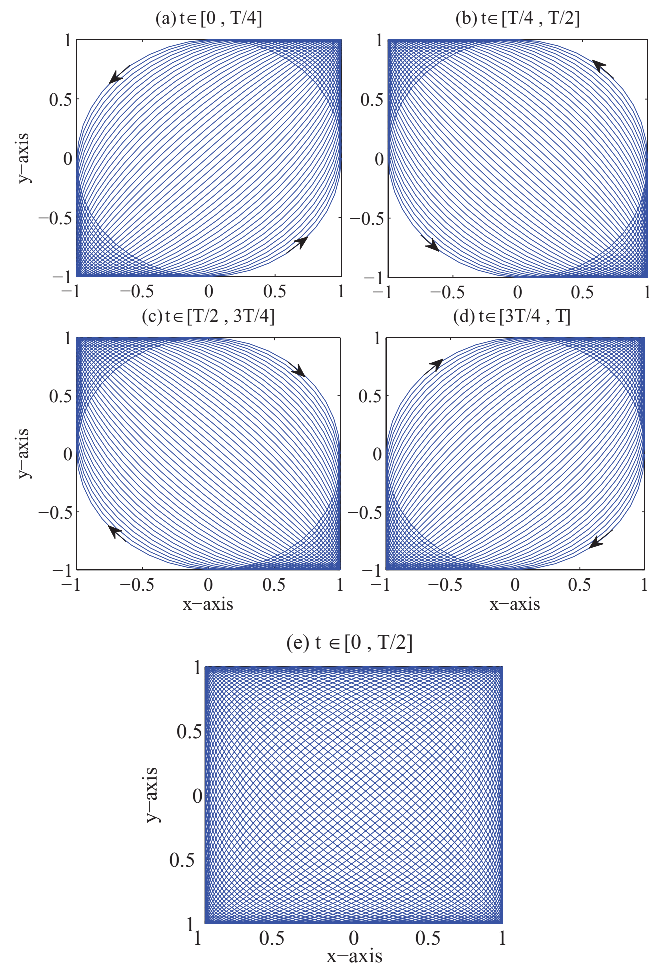

FIG. 1. Schematic of a Lissajous pattern. (a) The first quartered period, $0 \le t \le T/4$. The pattern evolves from a line to a circle (counter clockwise). (b) The second quartered period, $T/4 \le t \le T/2$. The pattern evolves from a circle to a line (counter clockwise). (c) The third quartered period, $T/2 \le t \le 3T/4$. The pattern evolves from a line to a circle (clockwise). (d) The fourth quartered period, $3T/4 \le t \le T$. The pattern evolves from a circle to a line (clockwise). (e) A square area can be fully scanned by a half-period Lissajous signal, $0 \le t \le T/2$.

shaped image. The full period of the Lissajous pattern is 1 s, which is calculated by the following relationship:[26]

$$T = \frac{1}{|f_x - f_y|}. \tag{2}$$

During the first quarter period, i.e., $0 \le t \le T/4$, the pattern evolves from a line to a circle. In the second quarter period ($T/4 \le t \le T/2$), the circle evolves back to a line. This transformation repeats itself in a reverse manner during the third and fourth quarter periods. Figure 1 shows the transformation of the Lissajous pattern.

As shown in Fig. 1(e), a square-shaped region can be fully scanned using a half-period Lissajous pattern. Although it is more efficient to use a quartered-period Lissajous since this will halve the total imaging time, a disadvantage of this approach is that the information in the vicinity of two diagonally opposing corners of an image is lost. However, it could be argued that this information may be insignificant in imaging applications, as often the central region of an image is of main interest. In this work, square-shaped images

Downloaded 04 Jun 2012 to 134.148.216.165. Redistribution subject to AIP license or copyright; see http://rsi.aip.org/about/rights_and_permissions

were recorded to demonstrate the effectiveness of the proposed scanning trajectory.

A. Analysis of Lissajous scan pattern

In this section, we present a rigorous analysis of the Lissajous pattern that leads to derivation of a measure of resolution. We assume that the Lissajous curve is enclosed by a rectangle defined by $(|x| \le A_x) \bigcap (|y| \le A_y)$ and that its x-y coordinates at time t are determined by Eq. (1). Assuming that the path has a fundamental period of T, then coprime positive integers k_x and k_y exist such that equalities $T = k_x T_x = k_y T_y$ are hold, where $T_x = 1/f_x$ and $T_y = 1/f_y$ are coordinate periods. Hence, the ratio of x and y frequencies should be a rational number, which is adopted as

$$\frac{f_x}{f_y} = \frac{2N}{2N-1}, \tag{3}$$

where N is a positive integer. Here, the frequency ratio is determined by one integer only, which further simplifies the design procedure compared to Ref. 26. Equation (3) also ensures that the path includes the lower right-hand corner of the rectangle. Since $2N$ and $2N-1$ are coprime, i.e., their greater common divisor is 1, k_x and k_y are equal to $2N$ and $2N-1$, respectively. Hence, the following relationships are obtained:

$$f_x = 2Nf; \quad f_y = (2N-1)f, \tag{4}$$

where $f = T^{-1} = f_x - f_y$ is the fundamental frequency of the path. In Appendix A, we show that the path traversed during the first half period is symmetric with respect to x-axis. Moreover, in the second half period, the previously traveled path during the first half period is traversed backward. In other words, no new path is traveled in the next half periods. Hence, with the selected frequencies and time profiles, the data during the time interval $t \in [0, \frac{T}{4}]$ are enough to reproduce the whole path. Moreover, the whole path is traversed once in each half period that starts from a multiple of $\frac{T}{2}$.

As shown in Fig. 1(e), the Lissajous curve is a closed path that intersects itself at many points. In this paper, the maximum distance between adjacent scan lines is considered as a measure of the image resolution. Before estimating the resolution measure, we calculate the positions of the crossing points, which are independent of the sampling frequency and simpler to obtain. However, for the resolution measure to be valid, we assume that the sampling frequency is high enough such that the distance between two successive sample points is sufficiently lower than the resolution measure.

As shown in Appendix B, the time interval between two successive crossing points located within the rectangle $(|x| \le A_x) \bigcap (|y| \le A_y)$ is a constant defined by

$$\Delta = \frac{1}{2f_y} - \frac{1}{2f_x} = \frac{1}{4N(2N-1)f}. \tag{5}$$

Moreover, the crossing points are traversed at time instants that are multiples of Δ.

Figure 2(a) shows the proposed Lissajous curve during the first half period with $N = 2$ and $A_x = A_y = 1$, along with the starting, ending, and crossing points. In this particular example, since N is very low, there are only three actual crossing

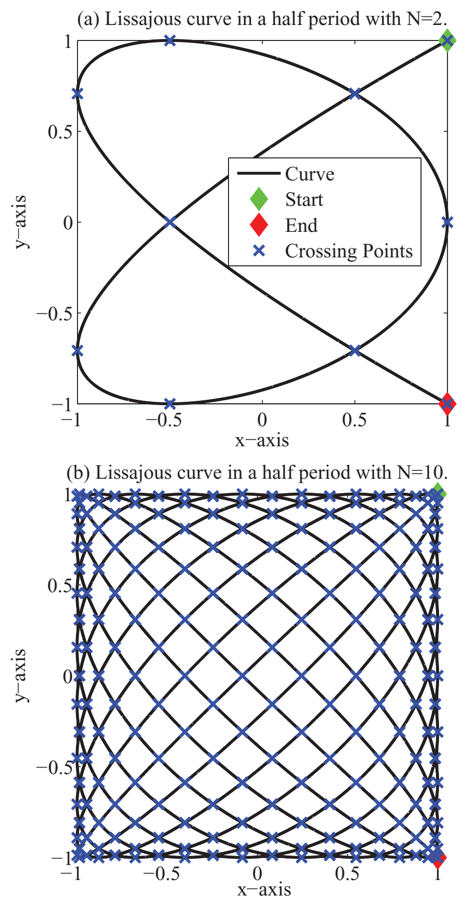

FIG. 2. (a) Lissajous pattern with $N = 2$, (b) with $N = 10$.

points, which is less than the number of edge points. However, for scanning applications, we use much higher values of N so that the number of actual crossing points is much higher than the number of points touching the rectangle sides, as shown in Fig. 2(b) with $N = 10$. Before obtaining the maximum distance between two adjacent scan curves as a measure of resolution, we consider the time instants corresponding to the absolute maximum of the speed, which is denoted as $t_{\max}$. Such time instants correspond to zones with the most widely spaced crossing points and can be used to determine a worst case resolution measure. In Appendix C, we show that for sufficiently large values of N, the local maxima approximately occur every $T/(4N)$ s, while the absolute maxima happen with a much longer period of $T/2$, approximately at the following time instants:

$$t_{\max} \cong \frac{4Nm \pm 1}{8Nf} = \frac{m \pm \frac{1}{4N}}{2f}, \quad m \in \{0, 1, 2, \ldots\}. \tag{6}$$

Using Eqs. (1), (4) and (6), the position corresponding to the absolute maximum speed can be determined as

$$x(t_{\max}) = 0, \quad y(t_{\max}) = \pm A_y \sin\left(\frac{\pi}{4N}\right) \approx 0, \tag{7}$$

where the plus sign is used when m is even, and *vice versa*. Equation (7) show that the maximum speed happens when the path is traversed very near the origin. In addition, the path is almost linear when the speed reaches its absolute maximum value (see the path in Fig. 2(b), around origin). During the

Downloaded 04 Jun 2012 to 134.148.216.165. Redistribution subject to AIP license or copyright; see http://rsi.aip.org/about/rights_and_permissions

scan, since the crossing points are met uniformly in each Δ s, the maximum spacing between two successive crossing points is associated with those that occur around $t = t_{\max}$. Hence, the lowest resolution zone is around the origin, where the path is almost linear. Using $m = 0$ with the plus sign in Eq. (6), the two nearest crossing points around the origin are passed at $t = (N-1)\Delta$ and $t = N\Delta$, and their coordinates can be written in the following form, respectively:

$$\begin{cases} x|_{t=(N-1)\Delta} = A_x \sin\left(\frac{\pi}{4N-2}\right) \\ y|_{t=(N-1)\Delta} = A_y \sin\left(\frac{\pi}{2N}\right), \end{cases} \tag{8}$$

$$\begin{cases} x|_{t=N\Delta} = -A_x \sin\left(\frac{\pi}{4N-2}\right) \\ y|_{t=N\Delta} = 0 \end{cases}. \tag{9}$$

After the foregoing points, the next two crossing points near the origin are around the local speed maximum that succeeds the absolute speed maximum. These crossing points happen at $t = 3N\Delta$ and $t = (3N-1)\Delta$ and have the following coordinates:

$$\begin{cases} x|_{t=(3N-1)\Delta} = A_x \sin\left(\frac{\pi}{4N-2}\right) \\ y|_{t=(3N-1)\Delta} = -A_y \sin\left(\frac{\pi}{2N}\right), \end{cases} \tag{10}$$

$$\begin{cases} x|_{t=3N\Delta} = -A_x \sin\left(\frac{3\pi}{4N-2}\right) \\ y|_{t=3N\Delta} = 0 \end{cases}. \tag{11}$$

Since N is large, the foregoing four crossing points around the origin form a diamond-like shape. The length of the diamond altitude, denoted by h, is a good approximation of the maximum distance between two adjacent scan lines. Hence, the altitude length is proposed as a measure of the resolution for the Lissajous scan, which is formulated in the following from:

$$h = \frac{4A_xA_y\cos^2\left(\frac{\pi}{4N-2}\right)\sin\left(\frac{\pi}{4N-2}\right)\sin\left(\frac{\pi}{2N}\right)}{\sqrt{4A_x^2\cos^4\left(\frac{\pi}{4N-2}\right)\sin^2\left(\frac{\pi}{4N-2}\right) + A_y^2\sin^2\left(\frac{\pi}{2N}\right)}} \approx \frac{\pi A_xA_y}{N\sqrt{A_x^2 + A_y^2}}. \tag{12}$$

B. Design steps for Lissajous scanning

Using the foregoing analysis, we may determine the Lissajous pattern parameters based on design priorities. For example, the following design steps can be adopted based on a predetermined raster dimensions, resolution, and x-axis frequency.

1. Assuming that the raster dimensions are known, A_x and A_y are determined.
2. Having selected a desired resolution h, the integer N can be approximately determined from Eq. (12), by rounding the expression $\frac{\pi A_xA_y}{h\sqrt{A_x^2+A_y^2}}$ to the nearest integer.
3. Based on the scanner limitations, select a suitable frequency for f_x such that the scanner can follow the corresponding sinusoidal references acceptably. Then, the path's fundamental frequency and f_y are obtained from Eq. (4) as $f = \frac{f_x}{2N}$ and $f_y = \frac{(2N-1)f_x}{2N}$.
4. The minimum scan time for the entire Lissajous pattern is a half period as $\frac{N}{f_x} \approx \frac{\pi A_xA_y}{f_xh\sqrt{A_x^2+A_y^2}}$.

III. EXPERIMENTAL RESULTS

In this section, efficacy of the Lissajous scanning method is investigated compared to the conventional raster scanning. More efficient implementation of the method is also presented using internal model controllers.

A. Lissajous versus raster scanning

We compare raster- and Lissajous-scanned images of a 8 μm × 8 μm region of a test grating on a commercial AFM (NT-MDT NTEGRA). The MikroMasch TGZ2 test grating has a repeating rectangular profile of 3 μm and 110 nm height. A cantilever with a resonance frequency of 78 kHz and a stiffness of 0.6 N/mm was used to perform the scans. This atomic force microscope uses a piezoelectric tube scanner with a resonance frequency of 825 Hz, whose open-loop measured frequency response with a unity dc gain is shown in Fig. 3 for x-axis direction. Here, we scaled x and y actuator signals such that the displacement outputs follow the associated inputs as closely as possible at sufficiently low frequencies. Hence, we can assign the unit of outputs (μm) to the manipulated inputs. The open-loop frequency response in y-axis direction, which is not shown for brevity, is almost identical to that of the x-axis. Experiments were conducted in open loop and in constant height contact mode. The x and y signals of the Lissajous trajectory were generated using a dSPACE-1103 rapid prototyping system. These signals were applied to a bipolar high voltage amplifier (NANONIS HVA4) with a gain of 15 in order to drive the piezoelectric tube scanner. A National

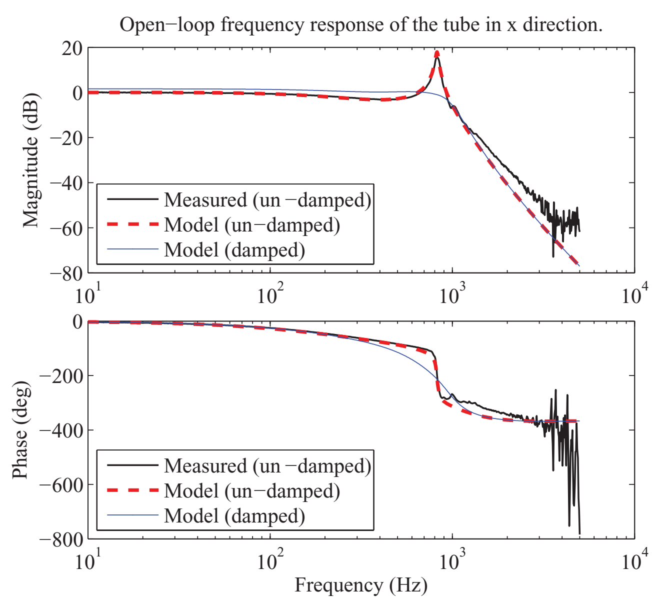

FIG. 3. Small signal open-loop frequency response of the piezoelectric tube scanner in x-axis direction along with an approximate fifth order linear model.

Downloaded 04 Jun 2012 to 134.148.216.165. Redistribution subject to AIP license or copyright; see http://rsi.aip.org/about/rights_and_permissions

TABLE I. Comparison of Lissajous and raster scanning rates adjusted for the same image resolution of 31.2 nm.

Scan time (s)	Imaging rate (frame/s)	Lissajous-scan frequency f_x (Hz)	Raster line rate (Hz)
28.5	0.035	10	8.98
3.17	0.315	90	80.76
1.425	0.7	200	179.65
0.475	2.11	600	538.94

Instruments PXI-6124 data acquisition card which has a sampling rate of 4 MS/s was used to record the images.

Assuming a scan dimension $A_x = A_y = 8\ \mu$m and an image resolution of $h = 31.2$ nm, the integer N for the Lissajous-scan method is equal to 285, which is comparable to that of a raster-scanned image with a pixel resolution of 256 × 256. Table I compares f_x with raster line rates that are required to complete images in 28.5 s (0.035 frame/s), 3.17 s (0.315 frame/s), 1.425 s (0.7 frame/s), and 0.475 s (2.11 frame/s). With $f_x = 90$ Hz, the image can be completed in 3.17 s by using the Lissajous-scan method. To obtain a raster-scanned image of similar resolution in approximately 3.17 s, the fast axis of the scanner is required to scan at 80.76 Hz line rate. This scan rate, which is excited by a triangular signal, will trigger the resonance frequency of the scanner and distort the AFM images.

To compare the image quality of the Lissajous and raster scan methods, images obtained by the two methods are shown in Figs. 4(a) and 4(b), respectively. Clearly, the image obtained by the Lissajous method has a better quality than that obtained by the raster scan, where the image was distorted due to vibrations. It can be observed that the image borders obtained by the open-loop methods considerably deviate from the exact rectangular frame associated with the coordinate signals in Eq. (1). Such deviations in the images, which results from poor tracking of scanner coordinates, can be improved using feedback control, as shown in Fig. 4(c), where we have used the IMC explained subsequently.

FIG. 4. 8 μm × 8 μm AFM images obtained at 0.315 frame/s. Images were completed in 3.17 s. (a) Open-loop Lissajous image. (b) Open-loop raster scan image. (c) Closed-loop Lissajous image.

B. Closed-loop control with IMC

In this section, we incorporate internal model controllers for x and y axes of the scanner. Internal model control is a well established method especially for tracking of constant, ramp, and sinusoidal reference signals.[28] In this method, the dynamic modes of the reference signal are incorporated in the controller. We used the block diagram shown in Fig. 5 for the x-axis of the scanner. A similar controller is also used for the y-axis. Because of some nonlinear and time-varying characteristics such as hysteresis and creep, the piezoelectric actuator deviates from linear operation.[9,29] These deviations increase with frequency and amplitude.[30] The nonlinearities can induce higher order harmonics of the sinusoidal references in the tracking error signal marked as e in Fig. 5. Hence, in addition to the poles associated with the reference sinusoids, we also include components with poles corresponding to some higher order harmonics of sinusoidal references in the compensators. The compensators $C_x(s)$ and $C_y(s)$ for x and y axes are described by the following equations:

$$C_x(s) = \frac{K_{ix}}{s} + \sum_{l=1(\neq 4)}^{5} \frac{K_{xl}(1+0.01s)}{1+\frac{s^2}{l^2\omega_x^2}}, \tag{13}$$

$$C_y(s) = \frac{K_{iy}}{s} + \sum_{l=1(\neq 4)}^{5} \frac{K_{yl}(1+0.01s)}{1+\frac{s^2}{l^2\omega_y^2}}. \tag{14}$$

For each reference frequency, the controller gains are tuned to obtain the best tracking errors. The scanner frequency

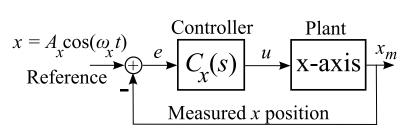

FIG. 5. Block diagram of feedback control system for x-axis.

Downloaded 04 Jun 2012 to 134.148.216.165. Redistribution subject to AIP license or copyright; see http://rsi.aip.org/about/rights_and_permissions

TABLE II. Lissajous-scan frequencies and IMC gains.

f_x(Hz) f_y(Hz)	K_{ix} K_{iy}	K_{x1} K_{y1}	K_{x2} K_{y2}	K_{x3} K_{y3}	K_{x5} K_{y5}
10	77.78	1.6	0	0.2	0
9.98	77.78	1.6	0	0.2	0
90	250	0.07	0.096	0.0064	0
89.84	250	0.07	0.096	0.0064	0
200	244	0.0115	0	−0.000213	0.0001
199.65	250	0.0103	0	−0.000191	0
600	500	−0.0057	0	0.000512	0
598.95	500	−0.0057	0	0.000512	0

responses for the x and y axes are reasonably similar and so are the coordinate frequencies ω_x and ω_y. Hence, for most reference frequencies, similar controllers are used for x and y axes.

Using the resolution, dimensions, and integer N as above, four different coordinate frequencies $f_x = 10$, 90, 200, and 600 Hz were chosen for constructing four Lissajous trajectories that were used to obtain the AFM images. The completion time for obtaining the four images are 28.5 s, 3.17 s, 1.425 s, and 0.475 s, respectively. Table II shows the coordinate frequencies along with the corresponding controller gains. For the first three frequency sets (10, 90, and 200 Hz), the box denoted *Plant* in Fig. 5 represents the open-loop tube. However, to provide adequate stability during the 600 Hz scan, where effects of nonlinearities and vibrations are more severe, we have to reduce the scan area to 5.5 μm × 5.5 μm and use damping loops to suppress the fundamental resonance of the tube. Hence, when applying reference sinusoids around 600 Hz, the *Plant* block in Fig. 5 represents the x-axis of the tube after the damping loop. The schematic diagram of the damping loop for x-axis is shown in Fig. 6. A similar damping loop structure is also used for the y-axis.

To design the damping loop, the x-axis frequency response was approximated by a fifth order transfer function having a unity dc gain and the following poles and zero:

$$\text{Poles} \in \{-1382, -103.6 \pm 5180i, -3195 \pm 5534i\},$$

$$\text{Zero} \in \{-12566\}\ \frac{\text{rad}}{\text{s}}.$$

The frequency response of the model, as shown in Fig. 3 with dashed curves, reasonably approximates the experimental data. To design the compensator in the damping loop, we use affine parametrization method[24] as described in Ref. 31. The desired poles selected for the damping loop (poles of the closed-loop system in Fig. 6) are

$$-10^3 \times [4, 5, 5, 7, 8 \pm 6i, 2 \pm 6i, 2 \pm 4i]\frac{\text{rad}}{\text{s}}. \qquad (15)$$

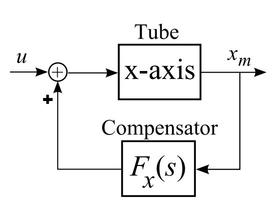

FIG. 6. Block diagram of damping loop for the x-axis of the tube.

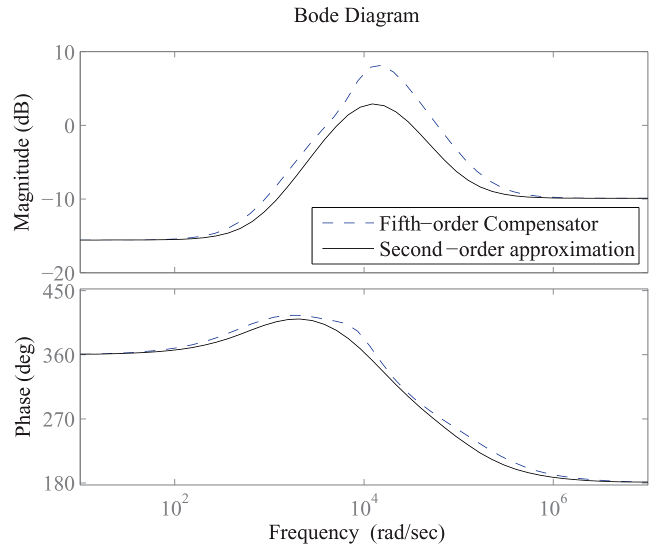

FIG. 7. Frequency responses of the damping compensator and its second-order approximation.

Before solving the associated pole assignment equation, the dc gain of the compensator is set to $\frac{1}{6}$. It was found that with the selected poles and dc gain, the resulting compensator has reasonably low gains and provides adequate stability margins for the loop. However, the compensator has the same order as that of the undamped model. Hence, we use a second-order approximation of the solution in the following form:

$$F_x(s) = \frac{-2 \times 10^{-9}s^2 + 0.0002239s + 0.1666}{6.258 \times 10^{-9}s^2 + 0.0001626s + 1}. \qquad (16)$$

The frequency responses of the resulting compensator and its second-order approximation are shown in Fig. 7. It turns out that the approximation further increases the stability margins of the loop. The damping loop has a gain margin of 12 dB, a phase margin of −70°, and the closed-loop frequency response shown in Fig. 3 (denoted by *damped model*). As the resulting damping compensator has a positive dc gain, it is almost consistent with positive position feedback control, which is a popular method of vibration suppression in flexible structures.[32]

The RMS values of the tracking errors are shown in Table III, in the columns marked as *Proposed IMC*. Note that the closed-loop RMS tracking errors for all four cases are

TABLE III. Experimental RMS tracking errors with the proposed and conventional IMC methods.

	Proposed IMC		Conventional IMC	
f_x(Hz)	X (nm) Y (nm)	X (%) Y (%)	X (nm) Y (nm)	X (%) Y (%)
10	4.4	0.05	22.8	0.28
	3.9	0.05	19.6	0.25
90	4.1	0.05	25.9	0.32
	5.2	0.06	25.6	0.32
200	17.1	0.21	30.7	0.38
	17.9	0.22	28.4	0.36
600	29.2	0.53	59.0	1.07
	27.0	0.49	55.3	1.00

Downloaded 04 Jun 2012 to 134.148.216.165. Redistribution subject to AIP license or copyright; see http://rsi.aip.org/about/rights_and_permissions

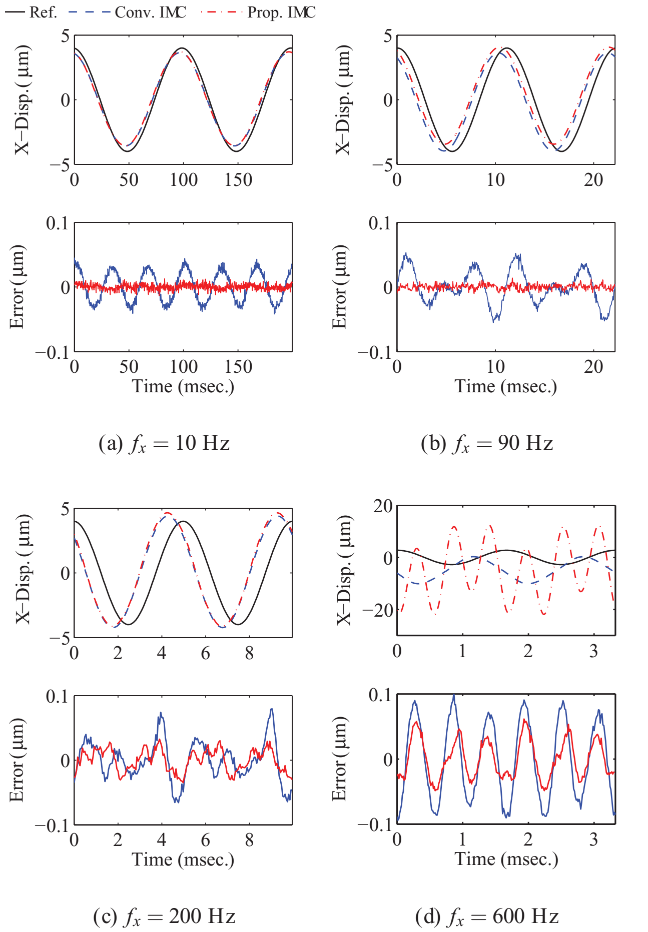

FIG. 8. Closed-loop tracking performances of IMCs at $f_x = 10$ Hz, $f_x = 90$ Hz, $f_x = 200$ Hz, and $f_x = 600$ Hz. X-displacement vs time plots: Reference signals are plotted in solid black lines; input signals of the conventional IMC to the plant are plotted in dashed lines (blue); and input signals of the proposed IMC to the plant are plotted in dash-dotted lines (red). Error vs time plots: Signals plotted in blue are error signals of the conventional IMC; and signals plotted in red are error signals of the proposed IMC designed to track higher harmonics of the reference sinusoids.

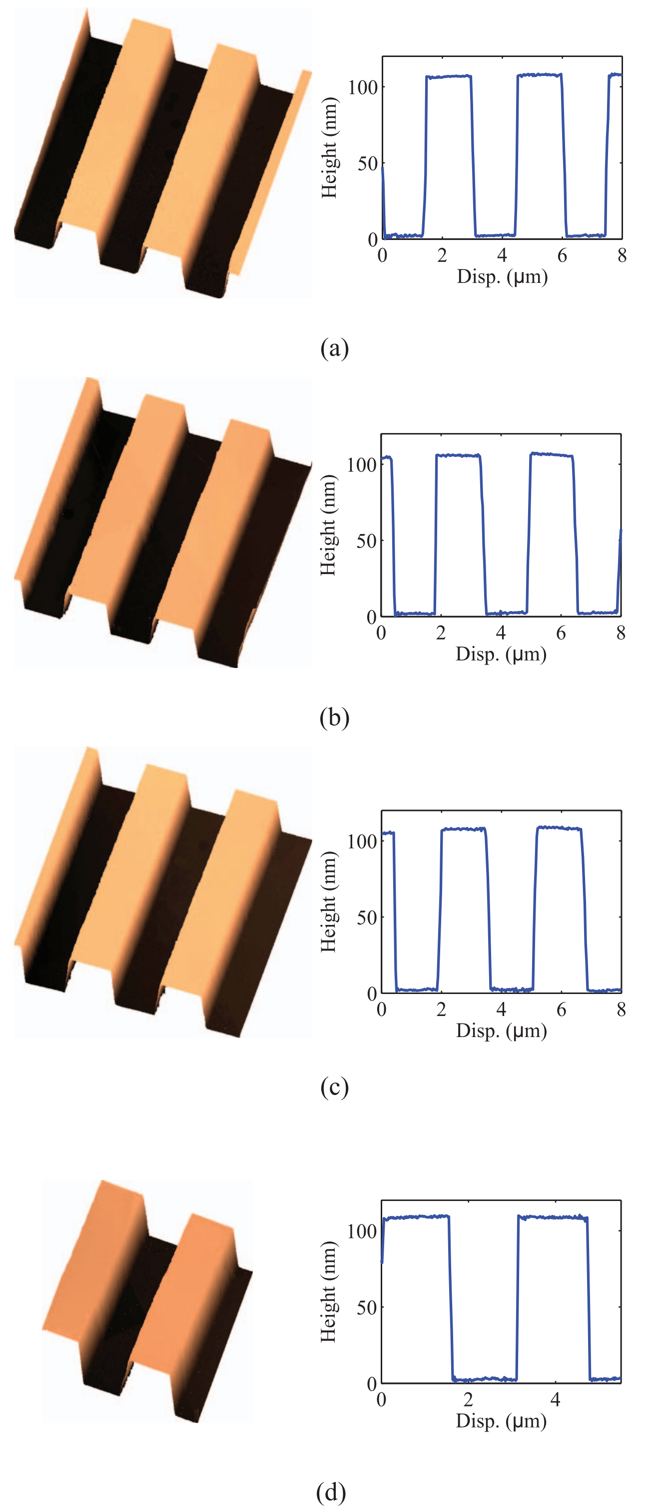

FIG. 9. Closed-loop AFM images and the corresponding Z profiles obtained using the proposed Lissajous trajectory with IMC implementation. (a) 28.5 s scan (at 0.035 frame/s, $f_x = 10$ Hz). (b) 3.17 s scan (at 0.315 frame/s, $f_x = 90$ Hz). (c) 1.425 s scan (at 0.7 frame/s, $f_x = 200$ Hz). (d) 0.475 s scan (at 2.11 frame/s, $f_x = 600$ Hz).

less than 0.53% of the full scan range. The closed-loop tracking performance is clearly superior to the open loop (shown in Fig. 4) which has a RMS error of 13.8%. The RMS values of tracking errors with conventional IMC method, i.e., when only the terms corresponding to the fundamental frequencies of the sinusoidal references are added to the integrators in the controllers, are also included in last two columns of Table III. Compared to the conventional IMC method, the proposed IMC method that includes higher order harmonic oscillators can considerably improve the tracking error. However, the degree of the improvement reduces as the frequency of the operation increases, which is due to more severe nonlinear behavior of the piezoelectric tube actuator at higher frequencies. The experimental time histories of the tracking errors, reference signals, and actuations of the x-axis are shown Fig. 8 for the conventional and the proposed methods, where the tracking errors with the proposed IMC method are almost at the noise level for 10 Hz and 90 Hz. As shown in Fig. 9, no distortion is visible in the AFM images obtained by the proposed IMC method for all four scans. It is worth stressing here that these results were obtained using a piezoelectric tube scanner which has the first mechanical resonance frequency at 825 Hz. Previous work shows that the maximum achievable raster imaging rate in closed loop is 0.032 frame/s.[33] In this work, imaging rates up to 2.11 frame/s were achieved where

Downloaded 04 Jun 2012 to 134.148.216.165. Redistribution subject to AIP license or copyright; see http://rsi.aip.org/about/rights_and_permissions

TABLE IV. Simulation results for tracking performances of x-axis using conventional integral controllers with the same noise rejection performance as that of the proposed IMC method.

f_x (Hz)	Noise rejection (%) $100\frac{x_{a\mathrm{RMS}}}{n_{\mathrm{RMS}}}\Big\vert_{x=0}$	Integral gain K_i	Tracking error (%) $100\frac{e_{\mathrm{RMS}}}{2A_x}\Big\vert_{n=0}$
10	4.8	280	7.8
90	19.5	2200	10.5
200	6.7	500	45
600	22	1110	42

high-quality AFM images were recorded. It would be difficult to achieve these scan results using the conventional raster trajectory.

C. Comparison with conventional integral control

One of the objectives of the feedback control systems in a nanopositioning application is to limit the closed-loop bandwidth from measurement noise n to real displacement x_a (see Fig. 5). This will ensure that the actual positioning error will be low. However, to acceptably track fast sinusoids in conventional feedback control systems such as proportional integral differential control, a high closed-loop bandwidth is usually required. This is a well known trade-off in control theory. A major benefit of the foregoing IMC methods in tracking of sinusoids is that they significantly improve the control performance while keeping the closed-loop bandwidth low. To illustrate this benefit, we drop all the terms corresponding to the harmonic oscillators in the controllers ($K_{xl} = K_{yl} = 0, \forall l$). However, we keep the integrators in $C_x(s)$ and $C_y(s)$, but adjust their gains such that the resulting control system has the same noise performance as that of the proposed IMC method. This is done by simulation using the x-axis model and a Gaussian random signal as the noise source n in Fig. 5, while the reference source x is zero, and the integrator gains are increased such that the RMS value of signal x_a in Fig. 5 remains the same as it was with the proposed IMC method. Table IV shows the noise rejection performances, the adjusted values of the integrator gains, and the resulting tracking errors associated with the reference sinusoids for x-axis. A comparison between these results and those of Table III clearly shows that using IMC controllers in Lissajous-scan method can improve the tracking error by a factor of 200 compared with the conventional integral control with the same level of measurement noise rejection.

IV. CONCLUSIONS

A Lissajous pattern was proposed for fast scanning applications along with a thorough mathematical analysis. The analysis led to a measure of resolution for the pattern and a systematic design procedure to determine the pattern parameters based on the desired resolution and scan speed. The method was successfully implemented on a commercial AFM platform and allowed capturing of high-quality images at much higher speeds than those achievable by the regular raster scan methods. We used a novel internal model control strategy to accurately track the sinusoidal references in the presence of actuator nonlinearities and sensor noise. Superiority of the proposed IMC method was shown by experiments compared to the conventional IMC method. It was shown by simulations that conventional integral control methods cannot compete with the IMC methods under the same noise rejection performance conditions.

ACKNOWLEDGMENTS

This work was performed in The Laboratory for Dynamics and Control of Nanosystems at The University of Newcastle Australia. The research was supported by the Australian Research Council and the University of Newcastle.

APPENDIX A

Using Eq. (4), we have $\frac{\omega_x T}{2} = 2\pi N$ and $\frac{\omega_y T}{2} = (2N - 1)\pi$, which ensures that equalities $x(\frac{T}{2} \pm t) = x(t)$ and $y(\frac{T}{2} \pm t) = -y(t)$ hold for all values of t. Hence, the path during the time interval $t \in [0, \frac{T}{2}]$ is symmetric with respect to the x-axis, i.e. $x(\frac{T}{4} + \tau) = x(\frac{T}{4} - \tau)$ and $y(\frac{T}{4} + \tau) = -y(\frac{T}{4} - \tau)$ for all τ. Also, one can easily show that the following equalities hold for all t:

$$x(T \pm t) = x(t); \quad y(T \pm t) = y(t). \tag{A1}$$

Therefore, in the second half period ($t \in [\frac{T}{2}, T]$), the previously traveled path in the first half period is traversed backward.

APPENDIX B

Assume a typical crossing point, which is met at times instants t_1 and t_2 ($t_2 > t_1 > 0$) and have to satisfy the following relationships:

$$t_2 \pm t_1 = K_x T_x, \tag{B1}$$

$$t_2 \pm t_1 = K_y T_y, \tag{B2}$$

where K_x and K_y are positive integers. The crossing points correspond to the nontrivial solutions of equations Eqs. (B1) and (B2), which can be summarized as $t_1 = K_1\Delta$ and $t_2 = K_2\Delta$, where K_1 and K_2 are positive integers defined as

$$K_1 = \left|2N(K_y - K_x) + K_x\right|, \tag{B3}$$

$$K_2 = 2N(K_y + K_x) - K_x. \tag{B4}$$

Hence, the crossing points occur at time instants that are multiples of Δ, and so is the time interval between two successive crossing points. Now, consider $t = k\Delta$ (k a positive integer) as a typical time instant, which is a multiple of Δ. Does it really correspond to a crossing point? To answer this question, one may consider non-negative integers q and r as the quotient and the remainder of k and $2N$ (i.e., $k = 2Nq + r$ with $r < 2N$) and use Eq. (B3) or (B4) to obtain positive integers K_x and K_y such that K_1 or K_2 becomes equal to k (e.g.,

Downloaded 04 Jun 2012 to 134.148.216.165. Redistribution subject to AIP license or copyright; see http://rsi.aip.org/about/rights_and_permissions

$K_x = r$ and $K_y = q + r$). One can easily show that for those values of k that are multiples of $2N$, the resulting K_x values are also multiples of $2N$. Similarly, when k is a multiple of $2N - 1$, so is the resulting K_y. In these cases, using equations Eqs. (4), (B1) and (B2), expression $t_2 \pm t_1$ becomes a multiple of the path period T; and from Eq. (A1), the curve traverses the same paths at times t_1 and t_2, and hence the points corresponding to those k values are not crossing points. Moreover, using Eqs. (1) and (4), such values of k, which are multiples of $2N$ and/or $2N - 1$, correspond to points that touch the sides of the rectangle, i.e., $|y(t)| = A_y$ and/or $|x(t)| = A_x$, respectively. Although, the aforementioned points are not actually crossing points, we include them among the crossing points for convenience and also to cover the points residing on the sides of the rectangle.

APPENDIX C

Using $v := \sqrt{\dot{x}^2 + \dot{y}^2}$ as the path speed and after some straightforward algebraic manipulations, the square of speed can be determined as

$$v^2(t) = V - A(t)\cos\left[2\omega_x t - \theta(t)\right], \tag{C1}$$

where

$$V = \frac{A_x^2\omega_x^2 + A_y^2\omega_y^2}{2}, \tag{C2}$$

$$A(t) = \sqrt{V^2 - A_x^2 A_y^2 \omega_x^2 \omega_y^2 \sin^2(\Omega t)}, \tag{C3}$$

$$\theta(t) = \arctan\left[\frac{A_y^2\omega_y^2 \sin(2\Omega t)}{A_x^2\omega_x^2 + A_y^2\omega_y^2\cos(2\Omega t)}\right]. \tag{C4}$$

Here, $\Omega := \omega_x - \omega_y = 2\pi f$ is the path frequency in rad/s. To simplify the analysis, we assume that N is large enough to ensure that the path frequency f is much smaller than the coordinate frequencies f_x and f_y (see Eq. (4)). Thus, the term $2\omega_x t$ in Eq. (C1) changes much faster than the amplitude $A(t)$ and phase $\theta(t)$, which depend on the slow term of Ωt. This helps to approximate the time instants of maximum speed by inspection. Consider a time interval around a specific time t such that $A(t)$ and $\theta(t)$ are almost constant but $\omega_x t$ can vary enough to make the cosine term in Eq. (C1) equal to -1, in an instant of the time interval. Hence, the local maximum speed around the arbitrary time t can be approximated by $V + A(t)$. Since $A(t)$ slowly changes with time according to Eq. (C3), the absolute maximum of speed should happen around time instances when the sine terms in Eqs. (C3) and (C4) vanish. In this way, at the time instants of absolute maximum speed, the phase angle $\theta(t)$ is almost zero and the speed is approximately equal to $\sqrt{A_x^2\omega_x^2 + A_y^2\omega_y^2}$. To approximate $t_{\max}$, we replace $\theta(t_{\max})$ by zero in equality $\cos\left[2\omega_x t_{\max} - \theta(t_{\max})\right] = -1$ to obtain the following solutions for the time instants of local maxima around the absolute maximum

$$t_{\max} \cong \frac{(2l+1)\pi}{2\omega_x} = \frac{2l+1}{8Nf}, \tag{C5}$$

where l is an integer. Eq. (C5) confirms that the local speed maxima approximately occur at the rate of $4Nf$. Among those local maxima, we are interested in the time instants corresponding to the absolute maxima, which approximately satisfy the equality of $\sin(\Omega t_{\max}) = 0$, i.e.,

$$t_{\max} \approx \frac{m\pi}{\Omega} = \frac{m}{2f}, \tag{C6}$$

where m is another integer. Eq. (C6) shows that the absolute maxima of speed occur at the slower rate of $2f$. The time interval between the local maxima is $\frac{1}{4Nf}$, while the interval between the absolute maxima is much larger ($\frac{1}{2f}$). Hence, it is possible to select local maxima whose time instants are very near to those of the absolute maxima. Thus, the odd integer of $2l + 1$ in Eq. (C5) should be selected as $4Nm \pm 1$ and more approximate solutions of $t_{\max}$ are obtained from Eq. (C5) in the form of Eq. (6).

[1] *Springer Handbook of Nanotechnology* edited by B. Bushan (Springer-Verlag, Berlin, 2004).
[2] G. Binnig and H. Rohrer, Helv. Phys. Acta **55**, 726 (1982).
[3] G. Binnig, C. F. Quate, and C. Gerber, Phys. Rev. Lett. **56**, 930 (1986).
[4] B. Hecht, H. Bielefeldt, Y. Inouye, D. W. Pohl, and L. Novotny, J. Appl. Phys. **81**, 2492 (1997).
[5] E. Eleftheriou, T. Antonakopoulos, G. Binnig, G. Cherubini, M. Despont, A. Dholakia, U. Durig, M. Lantz, H. Pozidis, H. Rothuizen, and P. Vettiger, IEEE Trans. Magn. **39**, 938 (2003).
[6] A. Sebastian, A. Pantazi, H. Pozidis, and E. Eleftheriou, IEEE Control Syst. Mag. **28**, 26 (2008).
[7] M. J. Rost, G. J. C. van Baarle, A. J. Katan, W. M. van Spengen, R. Schakle, W. A. van Loo, T. H. Oosterkamp, and J. W. M. Frenken, Asian J. Control **11**, 110 (2009).
[8] T. Ando, T. Uchihashi, and T. Fukuma, Prog. Surf. Sci. **83**, 337 (2008).
[9] S. Devasia, E. Eleftheriou, and S. O. R. Moheimani, IEEE Trans. Control Syst. Technol. **15**, 802 (2007).
[10] B. Bhikkaji and S. O. R. Moheimani, IEEE/ASME Trans. Mechatron. **13**, 530 (2008).
[11] Y. K. Yong, B. Arain, and S. O. R. Moheimani, Rev. Sci. Instrum. **81**, 033701 (2010).
[12] S. Aphale, S. Devasia, and S. O. R. Moheimani, Nanotechnology **19**, 125503 (2008).
[13] G. M. Clayton, S. Tien, K. K. Leang, Q. Zou, and S. Devasia, ASME J. Dyn. Syst., Measure., Control **131**, 061101 (2009).
[14] Y. K. Yong, S. Aphale, and S. O. R. Moheimani, IEEE Trans. Nanotechnol. **8**, 46 (2009).
[15] K. K. Leang and S. Devasia, IEEE Trans. Control Syst. Technol. **15**, 927 (2007).
[16] G. M. Clayton, S. Tien, A. J. Fleming, S. O. R. Moheimani, and S. Devasia, Mechatronics **18**, 273 (2008).
[17] G. Schitter, K. J. Astrom, B. E. DeMartini, P. J. Thurner, K. L. Turner, and P. K. Hansma, IEEE Trans. Control Syst. Technol. **15**, 906 (2007).
[18] T. Fukuma, Y. Okazaki, N. Kodera, T. Uchihashi, and T. Ando, Appl. Phys. Lett. **92**, 243119 (2008).
[19] Y. K. Yong and S. O. R. Moheimani, in *Proceeding of the IEEE/ASME International Conference on Advanced Intelligent Mechatronics, Montreal, Canada*, 6–9 July 2010.
[20] B. J. Kenton and K. K. Leang, IEEE/ASME Trans. Mechatron. **17**, 356 (2011).
[21] I. A. Mahmood and S. O. R. Moheimani, Nanotechnology **20**, 365503 (2009).
[22] I. A. Mahmood, S. O. R. Moheimani, and B. Bhikkaji, IEEE Trans. Nanotechnol. **10**, 203 (2011).
[23] Y. K. Yong, S. O. R. Moheimani, and I. R. Petersen, Nanotechnology **21**, 365503 (2010).
[24] G. C. Goodwin, S. F. Graebe, and M. E. Salgado, *Control System Design* (Prentice Hall, 2001).

Downloaded 04 Jun 2012 to 134.148.216.165. Redistribution subject to AIP license or copyright; see http://rsi.aip.org/about/rights_and_permissions

[25]S. O. R. Moheimani, Rev. Sci. Instrum. **79**, 071101 (2008).
[26]S. Moon, S.-W. Lee, M. Rubinstein, B. J. F. Wong, and Z. Chen, Opt. Express **18**, 21183 (2010).
[27]H. Moriguchi, M. Wendt, and J. L. Duerk, Magn. Reson. Med. **44**, 766 (2000).
[28]B. A. Francis and W. M. Wonham, Automatica **12**, 457 (1973).
[29]H. Jung, J. Y. Shim, and D. Gweon, Rev. Sci. Instrum. **71**, 3436 (2000).
[30]D. Song and C. J. Li, Mechatronics **9**, 391 (1999).
[31]A. Bazaei, Y. K. Yong, S. O. R. Moheimani, and A. Sebastian, IEEE Trans. Control Syst. Technol. **20**, 453 (2012).
[32]G. Song and B. N. Agrawal, Acta Astronaut. **49**, 73 (2001).
[33]A. J. Fleming, S. Aphale, and S. O. R. Moheimani, IEEE Trans. Nanotechnol. **9**, 438 (2010).

Downloaded 04 Jun 2012 to 134.148.216.165. Redistribution subject to AIP license or copyright; see http://rsi.aip.org/about/rights_and_permissions